Transport and losses of energetic particles in tokamaks in the presence of Alfvén activity using the new full orbit TAPaS code coupled to FAR3d

H Betar, David Zarzoso, Jacobo Varela, Diego Del-Castillo-Negrete, Luis Garcia, Xiaodi Du

Transport and losses of energetic particles in tokamaks in the presence of Alfvén activity using the new full orbit TAPAS code coupled to FAR3d

Betar, H.‡

Aix Marseille Univ, CNRS, Centrale Med, M2P2 UMR 7340, Marseille, France

E-mail: homam.betar@renfusion.eu

Zarzoso, D.

Aix-Marseille Univ, CNRS, Centrale Med, M2P2 UMR 7340, Marseille, France

E-mail: david.zarzoso-fernandez@cnrs.fr

Varela, J.

Institute for Fusion Studies, Department of Physics, University of Texas at Austin, Austin, Texas 78712, USA

Del-Castillo-Negrete, D.

Oak Ridge National Laboratory, Oak Ridge, TN 37831-8071, United States of America

Garcia, L.

Universidad Carlos III de Madrid, 28911 Leganes, Madrid, Spain

Du, X.

General Atomics, P.O. Box 85608, San Diego, California 92186-5608, USA

Abstract. Recent developments and tools integrated into the TAPAS code are presented, enabling realistic scenario simulations of particle dynamics within experimental tokamak magnetic equilibria. In particular, the enhanced capabilities of TAPAS enable seamless coupling with external simulations, provided the metric and equilibrium magnetic field of the external code are known. Coupling TAPAS with the gyro-fluid code FAR3d, the transport and losses of energetic particles (EPs) in the presence Alfvén eigenmodes (AEs) in DIII-D plasma discharge #159243 were investigated. Detailed analyses of prompt losses with and without collisions were performed. Then, further analysis was performed in the presence of electromagnetic perturbations resulting from AEs activity. The results indicate that, for the energies and the initial conditions considered here, the presence of AEs enhances the particle losses.

‡ Present address: Renaissance Fusion, 38600 Fontaine, France

1. Introduction

In current and future fusion devices, energetic particles (EPs) play a crucial role. These particles are generated either externally from sources such as neutral beam injection (NBI) and ion cyclotron resonance heating (ICRH), or internally through nuclear fusion reactions, resulting in 3.5 MeV alpha particles from D-T fusion reactions. It is imperative to adequately confine EPs to ensure the transfer of their energy to the thermal population via Coulomb collisions, thereby sustaining fusion reactions. Hence, the necessity to investigate the transport phenomena associated with EPs in toroidal plasmas. Additionally, EPs in toroidal plasmas can trigger instabilities, particularly EP-driven modes, which might have deleterious effects on the energy and particle confinement.

EP-driven instabilities involve various phenomena, such as the fishbone instability initially observed in the PDX tokamak [1], later analyzed in DIII-D plasma [2], and shear Alfvén eigenmodes destabilized by super-Alfvénic EPs. These modes can lead to major EP losses towards the plasma-facing components, as demonstrated for energetic beam ions and byproducts of D-D fusion reactions in the DIII-D tokamak [3, 4]. Shear Alfvén waves usually experience strong continuum damping in slab and cylindrical geometries in the presence of non-uniform magnetic field, with the exception of global Alfvén eigenmodes (GAE) in cylindrical geometry arising below the minimum value in the Alfvén contiuum [5, 6, 7, 8].

However, in realistic toroidal geometry with noncircular flux surfaces, gaps in the Alfvén continuum can be formed, leading to the existence of eigenmodes that are not damped by the continuum. Those include toroidicity induced Alfvén eigenmodes (TAE) [9, 10], ellipticity induced Alfvén eigenmodes (EAE) [11, 12], noncircularity induced Alfvén eigenmodes (NAE) [13, 14], reversed-shear Alfvén eigenmodes (RSAE)[15, 16], and beta-induced Alfvén eigenmodes (BAE) [17] - for more details, see Ref. [18] and references therein. Since modes inside these gaps are not damped by the continuum, any external drive at the corresponding frequencies can provide enough energy to trigger an instability. More specifically, the motion of EPs can resonate with these modes and the gradients of the EP distribution function in phase-space can result in their destabilization. This is why they can be excited by alpha particles resulting from fusion reactions or by EPs generated through NBI or ICRH -see Ref [19] and references therein. Moreover, different types of EP transport exist in toroidal plasmas [20].

The dynamics of EPs can be numerically analyzed following two approaches: active coupling and passive coupling. The active coupling approach employs a self-consistent model for EPs and thermal particles. This includes, for example, fully kinetic (or gyrokinetic) description of both the thermal plasma and EPs, hybrid models where different equations are solved for the thermal plasma and the EPs (e.g. Ref[21]), and gyro-fluid models, which are derived by taking moments of the gyrokinetic equation and applying appropriate closures [22]. In the second approach, passive-tracers codes are used. In this case, the time-dependent electromagnetic perturbations are externally

imposed and the trajectories of EPs are integrated but do not impact the evolution of the perturbations. Some of these codes, which can be regarded as diagnostic tools, are ASCOT [23], LOCUST [24], ORBIT [25], or KORC [26]. TAPAS code [27] falls in this category and can be easily coupled to solvers that evolve the dynamics of the background plasma. The present paper introduces the new updates implemented in TAPAS, and focuses on performing an in-depth investigation of EP transport and losses in the presence of the 3D electromagnetic perturbations induced by Alfvén eigenmodes. Our investigation focuses on the experimental equilibrium of the DIII-D tokamak calculated for the plasma discharge #159243 [28]. In this discharge, EPs are generated by NBI with energies of the order of ~ 20 keV. The evolution of the electromagnetic perturbations is modeled using the gyro-fluid code FAR3d [22].

The remainder of the paper is structured as follows. Section 2 details the last upgrades that have been implemented in TAPAS code, namely the full-orbit integration, the use of experimental magnetic equilibrium, the interpolation methods parallelized using GPUs, the inclusion of collisions and the numerical performance of the whole workflow comparing CPU and GPU parallelizations. Section 3 is devoted to presenting the results of the simulations using FAR3d code, which provides the electromagnetic perturbations to be used in TAPAS in section 4. Finally, we give a summary and directions for future research in section 5.

2. Description of the full-orbit TAPAS code

The Toroidal Accelerated PArticle Simulator (TAPAS) code has undergone significant updates since its initial version [27]. The previous version only integrated trajectories in a 5-dimensional guiding-center coordinate system, whereas the current version now possesses the capability to track particle dynamics in a 6-dimensional phase space $(\mathbf{x}, \mathbf{v})$, where $\mathbf{x} = (x, y, z)$ and $\mathbf{v} = (v_x, v_y, v_z)$ represent the position and velocity components of the particle, respectively, which allows for the resolution of the particle gyro-motion.

Moreover, unlike the initial version of TAPAS, which assumed simplified concentric and circular flux surfaces for numerical convenience and analytical solution for electromagnetic perturbation, the updated version is capable of handling realistic axisymmetric equilibria. Consequently, magnetic equilibria obtained using equilibrium codes such as VMEC [29, 30], DESC [31], and SIESTA [32] can be seamlessly incorporated into TAPAS by reading the equilibrium fields from an external file. Additionally, particle trajectories are integrated in the presence of electromagnetic fields obtained from external codes, like FAR3d, which is employed in this paper for the analysis of transport and losses of energetic particles. It is to be noted that due to the use of experimental equilibria and external fields, interpolation methods are essential. In TAPAS, we use Lagrange polynomials for interpolation in 1D and 2D, whereas B-splines are used for interpolation of the electromagnetic field in 3D. B-splines are preferred for 3D field interpolation owing to their enhanced stability and robustness to numerical oscillations. This is partially attributed to the smoothness and local support

of the basis functions, which enable precise control over the influence of nearby data points. Moreover, the B-spline interpolation scheme is formulated in generalized toroidal geometry, making it a versatile tool. To enhance the performance of the code, 3D B-splines have been parallelized and GPU-accelerated.

2.1. Integration of particle trajectories

Assuming no collisions, the equations solved by the full-orbit version of TAPAS are

$$\frac{\mathrm{d}x_i}{\mathrm{d}t} = v_i \tag{1}$$

$$m_s \frac{\mathrm{d}v_i}{\mathrm{d}t} = eZ_s \left(E_i + \epsilon_{ijk} v_j B_k\right) \tag{2}$$

where the Einstein summation notation has been used. In the previous equations, e is the elementary charge, Z_s and m_s are the atomic number and the mass of the particle, respectively, $x_i = x, y, z$, and $v_i = v_x, v_y, v_z$ are the position and velocity components of the particle, and ϵ_{ijk} is the Levi-Civita symbol. E_i and B_i are the i^{th} components of the electric and magnetic fields at the particle position obtained, in this paper, using FAR3d code. The Boris method is employed to integrate numerically the equations of motion. It is a second-order leapfrog scheme generally used due to its long-term accuracy and its ability to effectively resolve the gyro-motion of particles. One notable advantage of the Boris method is its energy conservation property, making the Boris algorithm a standard choice for particle pushing in particle-in-cell (PIC) codes used to solve the Boltzmann-Maxwell system of equations in plasma physics [33]. Eqs.(1) and (2) are discretized in time as follows

$$\frac{x_i^{n+1} - x_i^n}{\Delta t} = v_i^{n+\frac{1}{2}} \tag{3}$$

$$\frac{v_i^{n+\frac{1}{2}} - v_i^{n-\frac{1}{2}}}{\Delta t} = eZ_s E_i(\mathbf{x}^n) + eZ_s \epsilon_{ijk} \frac{v_j^{n+\frac{1}{2}} + v_j^{n-\frac{1}{2}}}{2} B_k(\mathbf{x}^n) \tag{4}$$

where Δt is the time step. Eqs.(1) and (2) are approximated at times $t_{n+1/2}$ and t_n, respectively. The electromagnetic fields are evaluated at the particle position at time t_n. The velocity is evaluated as the average of its values at $t_{n+1/2}$ and $t_{n-1/2}$. The electric field in Eq.(4) can be eliminated by splitting the calculation into three steps: two acceleration steps due to the electric field and one pure rotation due to the magnetic field. This is achieved by defining $v_j^{n-\frac{1}{2}}$ and $v_j^{n+\frac{1}{2}}$ as follows

$$v_j^{n-\frac{1}{2}} = v_j^- - \frac{eZ_s E_j}{m_s} \frac{\Delta t}{2}, \qquad v_j^{n+\frac{1}{2}} = v_j^+ + \frac{eZ_s E_j}{m_s} \frac{\Delta t}{2} \tag{5}$$

which leads, after substituting in Eq.(4), to

$$v_j^+ = v_j^- + \epsilon_{jmn} \tilde{v}_m s_n \tag{6}$$

where

$$\tilde{v}_m = v_m^- + \epsilon_{mnl} v_n^- Q_l, \qquad Q_l = \frac{eZ_s B_l}{m_s} \frac{\Delta t}{2}, \qquad s_n = \frac{2Q_n}{1 + Q^2} \tag{7}$$

It should be noted that TAPAS can also integrate the trajectories of guiding-centres. The set of equations and the numerical scheme were presented in [27]. Finally, in TAPAS, various methods for initializing particles in velocity space have been implemented. One can provide the initial conditions using four different descriptions: $(v_\parallel, \mu)$, (E, Λ), (E, λ) and (E, P_φ). Here E is the kinetic energy, $\Lambda = \mu B_0/E$, $\lambda = v_\parallel/v$, and $P_\varphi = -eZ_s\psi + m_s R v_\varphi$. Consequently, if the initial velocities are given in one of these spaces, TAPAS calculates the corresponding (v_x, v_y, v_z) for particles since the Boris algorithm solves the equations of motion in Cartesian geometry. Moreover, to account for the initialization following specific distribution functions, the possibility exists to initialize particles in phase space by means of the Metropolis-Hastings algorithm based on the Markov chain Monte-Carlo method [34, 35, 36].

The integration of trajectories in the absence of collisions has been tested by initializing a set of particles at the same position $r = 75\rho_{\text{ref}}$ with parallel velocity $-6v_{\text{th}} \leq v_\parallel \leq 6v_{\text{th}}$ and magnetic moment $0 \leq \mu \leq 18T_{\text{ref}}/B_0$ for an equilibrium calculated with the VMEC code [37] for the plasma discharge #159243 of DIIID tokamak (see Section 3). The different trajectories observed have been identified and represented in Fig. 1a. The blue points correspond to trapped particles (identified as they reverse the sign of the parallel velocity). The yellow region outside the trapping zone represents passing particles, whereas the yellow region within the blue zone indicates stagnation orbits. These stagnation orbits correspond to particles that do not reverse the sign of their parallel velocity and exhibit minimal evolution in the poloidal angle. The dashed black line represents the theoretical passing-trapping boundary, assuming that particles remain on their initial magnetic flux surface and that the magnetic field follows the form $B \propto (1 + \epsilon\cos\theta)^{-1}$.

Trapped particles initialized with negative parallel velocity closely follow the theoretical boundary, whereas a significant deviation is observed for those initialized with positive parallel velocity. This is due to the conservation of the toroidal canonical momentum, which makes particles explore different magnetic surfaces, which is called the orbit width Δ_{orbit}. Those with initial negative parallel velocity explore the inner region of the tokamak with smaller Δ_{orbit} than those with initial positive parallel velocities, which explore the outer region. Moreover, for the inner magnetic surfaces, the assumption $B \propto (1 + \epsilon\cos\theta)^{-1}$ is a good approximation. On the same figure, six squares have been plotted, representing six different particles for which the poloidal cross sections of the trajectories have been shown in Fig. 1b. The particles are identified by the same colors in the figures. An inset is also provided showing the stagnation trajectory (red particle). Figs. 1c and 1d illustrate the time evolution of the kinetic energy and the toroidal canonical momentum, respectively, for each of the six identified particles, showing good conservation properties of the numerical scheme.

As a benchmark, we compare in Fig. 2 two trajectories: one calculated with the full-orbit version and one with the guiding-centre one (see Eqs. in [27]). The projection onto the poloidal cross section of two types of trajectories (passing and trapped) are plotted. Both particles have equal initial energies: $E_{\text{EP}} = 4E_{\text{th}}$, where E_{th} is the reference

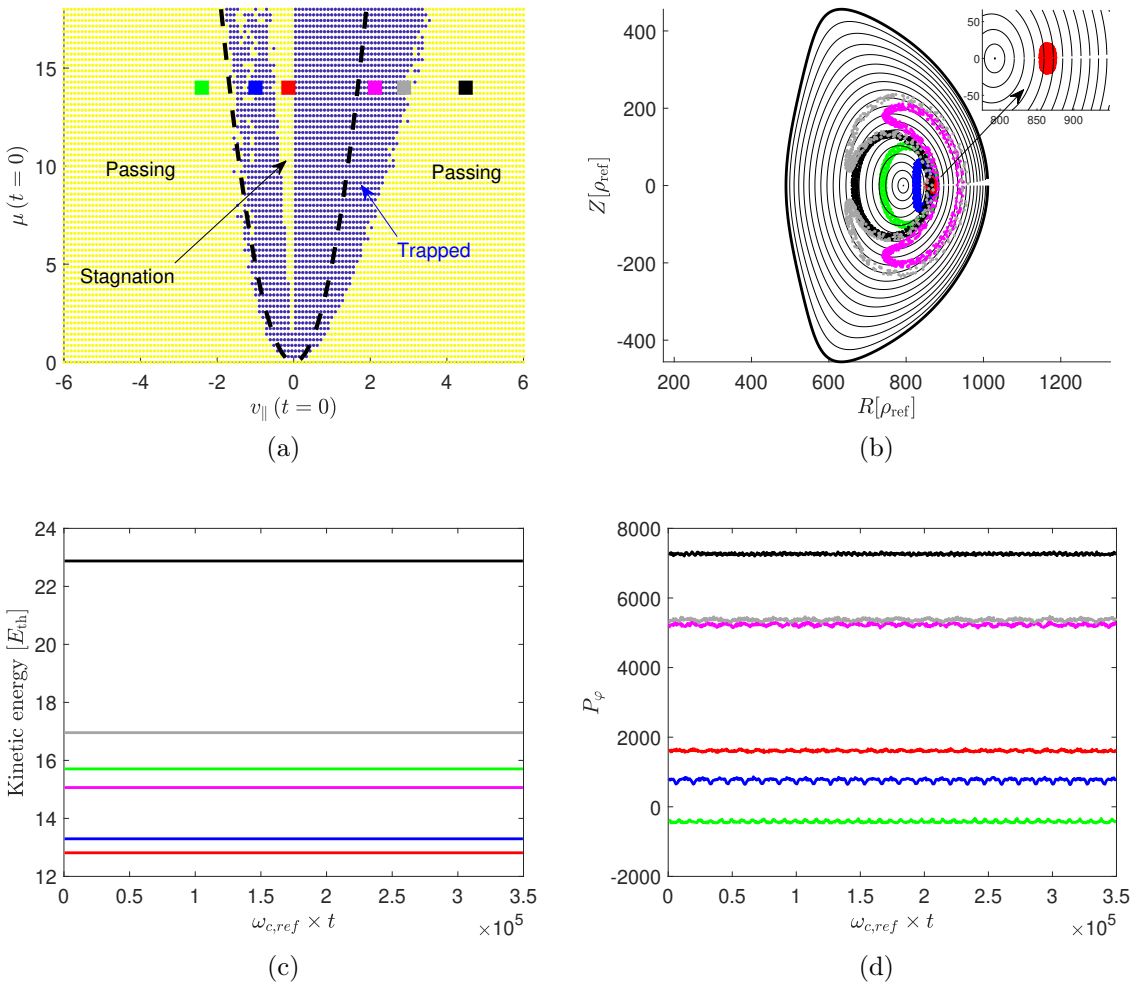

Figure 1: (a) Classification of trajectories as a function of the initial parallel velocity and magnetic moment together with six particles selected for visualization. (b) Projection onto the poloidal cross-section of the trajectories of the six selected particles, together with an inset for the stagnation orbit. Time trace of the kinetic energy (c) and toroidal canonical momentum (d) for the six particles.

thermal energy. While both particles were initialized at $\theta = 0$ and $\varphi = 0$, their radial initialization differs, with the passing particle at $r = 170\rho_{\rm ref}$ and the trapped particle at $r = 50\rho_{\rm ref}$, where $\rho_{\rm ref}$ denotes the reference Larmor radius. The initial conditions of the particles (low energy and small Larmor radius) must result in guiding-centre and full-orbit trajectories very close to each other. This is evidenced by Fig. 2, where the blue and red curves represent the trajectories for the full orbit and for the guiding-centre versions, respectively.

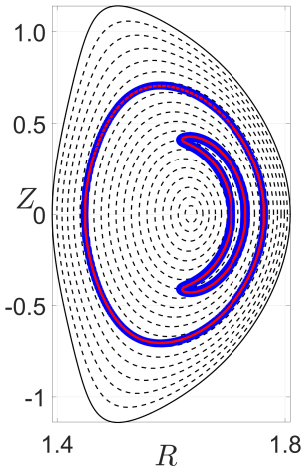

Figure 2: Trajectories of a passing particle and a trapped banana particle, obtained using both the full orbit (blue curves) and guiding-centre (red curves) versions of TAPAS.

2.2. Collision operator

Collisions are introduced in TAPAS by means of a stochastic operator and a deterministic operator, which model the diffusion and the Coulomb drag, respectively, for test particles colliding with background particles of mass m_b, charge eZ_b, density n_b and temperature T_b. For the case of background electrons, we have $b = e$, whereas for background ions $b = i$. The reader can find a detailed description and derivation of the collision operator in plasma physics textbooks such as [38, 39]. The equations governing the evolution of the velocity in the presence of collisions are

$$\mathrm{d}\mathbf{v}_{\mathrm{coll,\,det}} = -\nu_s \mathrm{d}t \tag{8}$$

$$\mathrm{d}\mathbf{v}_{\mathrm{coll,\,stoch}} = \left[\sqrt{D_\parallel}\frac{\mathbf{v}\otimes\mathbf{v}}{v^2} + \sqrt{D_\perp}\left(\mathbf{I} - \frac{\mathbf{v}\otimes\mathbf{v}}{v^2}\right)\right]\cdot \mathrm{d}\mathbf{W}^{\mathbf{v}} \tag{9}$$

where $\mathbf{W}^{\mathbf{v}}$ is a Wiener process in velocity space and $\mathbf{I}$ is the unit tensor in 3D.

In the deterministic part of the collision operator, ν_s represents the Coulomb drag given by the expression

$$\nu_s = \sum_b 4n_b C_b \left(\frac{m_b}{2k_B T_b}\right)^{3/2} \frac{\psi(x)}{x} \tag{10}$$

with k_B the Boltzmann constant, C_b given by the expression

$$C_b = \frac{e^2 Z_s^2 e^2 Z_b^2 \log\Lambda}{8\pi\epsilon_0^2 m_s^2} \tag{11}$$

the variable x is defined by

$$x = \frac{v}{\sqrt{T_b/(2m_b)}} \tag{12}$$

and the function ψ is defined as

$$\psi(x) = \frac{\Phi(x) - x\Phi'(x)}{2x^2} \tag{13}$$

with Φ the error function

$$\Phi(x) = \frac{2}{\sqrt{\pi}} \int_0^x \mathrm{e}^{-u^2} \mathrm{d}u \tag{14}$$

In the stochastic part, $D_\parallel$ and $D_\perp$ are the diffusion coefficients, calculated as follows

$$D_\parallel = \sum_b 4 n_b C_b \left(\frac{m_b}{2 k_B T_b} \right)^{1/2} \frac{\psi(x)}{x} \tag{15}$$

$$D_\perp = \sum_b 2 n_b C_b \left(\frac{m_b}{2 k_B T_b} \right)^{1/2} \frac{\Phi(x) - \psi(x)}{x} \tag{16}$$

The deterministic part is solved after each update of the velocity in the Boris algorithm, using the same strategy as the one used in [26] for the radiative term of runaway electrons. In practice, the deterministic equation is decomposed into the effect of the Lorentz force $\mathrm{d}\mathbf{v}_{\mathrm{L,\,det}} = eZ_s/m_s \left(\mathbf{E} + \mathbf{v} \times \mathbf{B}\right)$ and the effect of collisions $\mathrm{d}\mathbf{v}_{\mathrm{coll,\,det}} = -\nu_s \mathrm{d}t$. At each time step i, the velocity due to the Lorentz force at the time step $i+1$ is computed. The result of this computation is called $\mathbf{v}_{\mathrm{L}}^{i+1}$. The effect of the Coulomb drag is then computed as follows

$$\frac{\mathbf{v}_{\mathrm{coll,\,det}}^{i+1} - \mathbf{v}^i}{\Delta t} = \nu_s \left(\mathbf{x}^{i+1/2}, \mathbf{v}^{i+1/2} \right) \mathbf{v}^{i+1/2} \tag{17}$$

with $\mathbf{v}^{i+1/2} = \left(\mathbf{v}_{\mathrm{L}}^{i+1} + \mathbf{v}^i\right)/2$. The new velocity is then computed as

$$\mathbf{v}^{i+1} = \mathbf{v}_{\mathrm{L}}^{i+1} + \mathbf{v}_{\mathrm{coll,\,det}}^{i+1} - \mathbf{v}^i \tag{18}$$

The stochastic part is solved using the Euler scheme, with a time step larger than the one used for the integration of the deterministic equations in order to reduce the computational time. The Wiener process is generated taking into account that it must have independent and Gaussian increments. Therefore, the increment $\mathrm{d}\mathbf{W}^{\mathbf{v}}$ is generated using a Box-Muller algorithm for each direction (x, y, z).

The collision operator has been tested initializing an ensemble of 10^6 particles at the same position in real space with velocities localized around $v_\parallel = 2$ and $v_\perp = 2$. The initialization in velocity space is illustrated in Fig.3a. The colormap represents the distribution function computed from the initial particles and the dashed lines represent as a reference the Maxwellian distribution function. After $\omega_{c,0} t = 10^7$, the distribution function is recomputed. The result is illustrated in Fig.3b. A very good agreement is obtained. Such agreement becomes evident when plotting the distribution function for a given value of μ and for a given value of $v_\parallel$, which is shown in Figs. 3c and 3d, respectively.

2.3. Performance of the parallel algorithm of TAPAS

The simulations presented in this work were performed on the French Jean-Zay supercomputer (HPE SGI 8600 system), with CPU and GPU partitions. The CPU

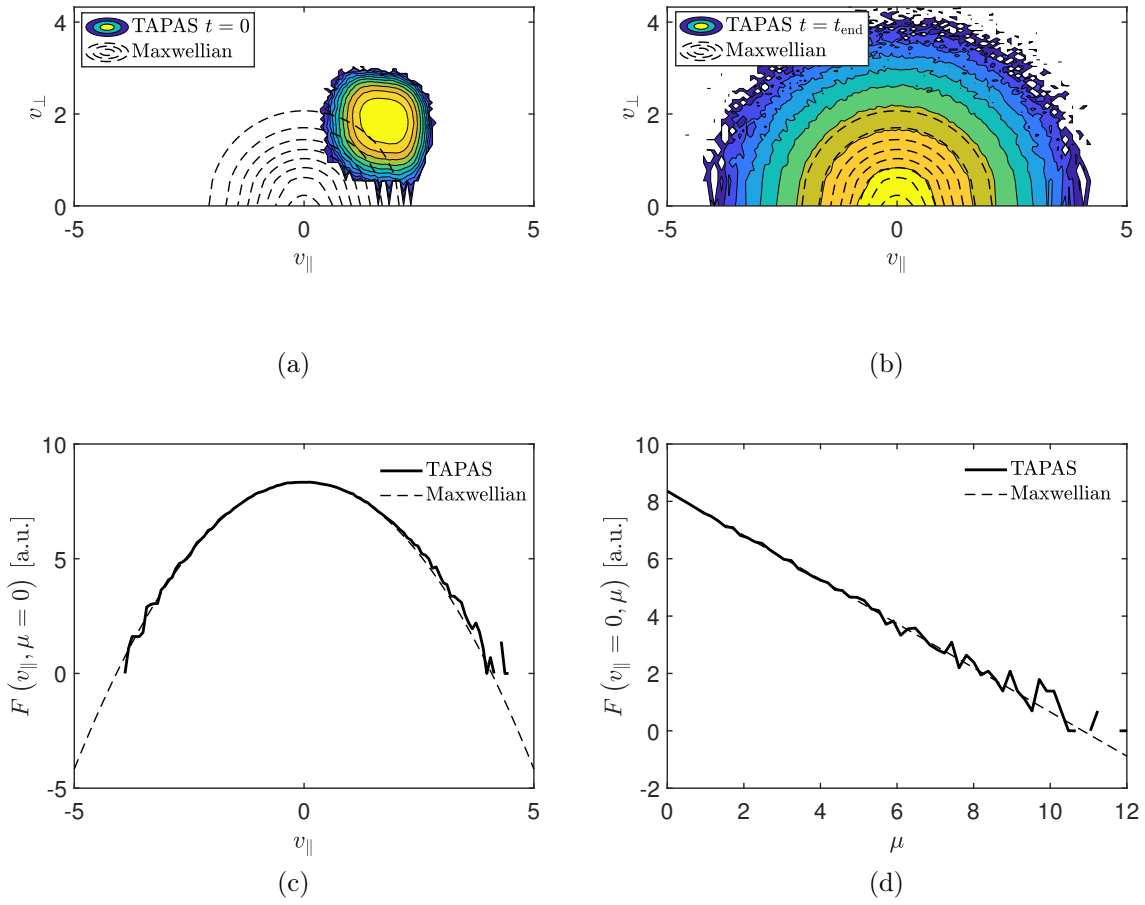

Figure 3: Initial (top left) and final (top right) distribution functions in $(v_\parallel, v_\perp)$ computed from TAPAS in the presence of collisions. As a reference, the Maxwellian distribution is provided using contour plot. Also, in the same figure, the final distribution function for a given value of μ (bottom left) and for a given value of $v_\parallel$ (bottom right) is given as a function of $v_\parallel$ and μ, respectively. The Maxwellian distribution is given using dash line.

partition employed for this paper consists of 1528 compute nodes, each equipped with 2 Intel Cascade Lake processors (20 cores per processor and 192 GB of shared memory per node). The accelerated nodes consist of 2 processors (20 cores each) and 4 NVIDIA Tesla V100 GPUs, each equipped with 32GB of memory. The compute nodes are interconnected by an Intel Omni-Path network (OPA). Scaling analyses were performed for a fixed-size problem to test different situations. In particular, we focus on the impact of B-spline interpolation on the overall performance when integrating the particle trajectories in the presence of $3D$ electrostatic perturbation calculated by the GYSELA code [40] to study electrostatic kinetic turbulence. We also investigate the effects

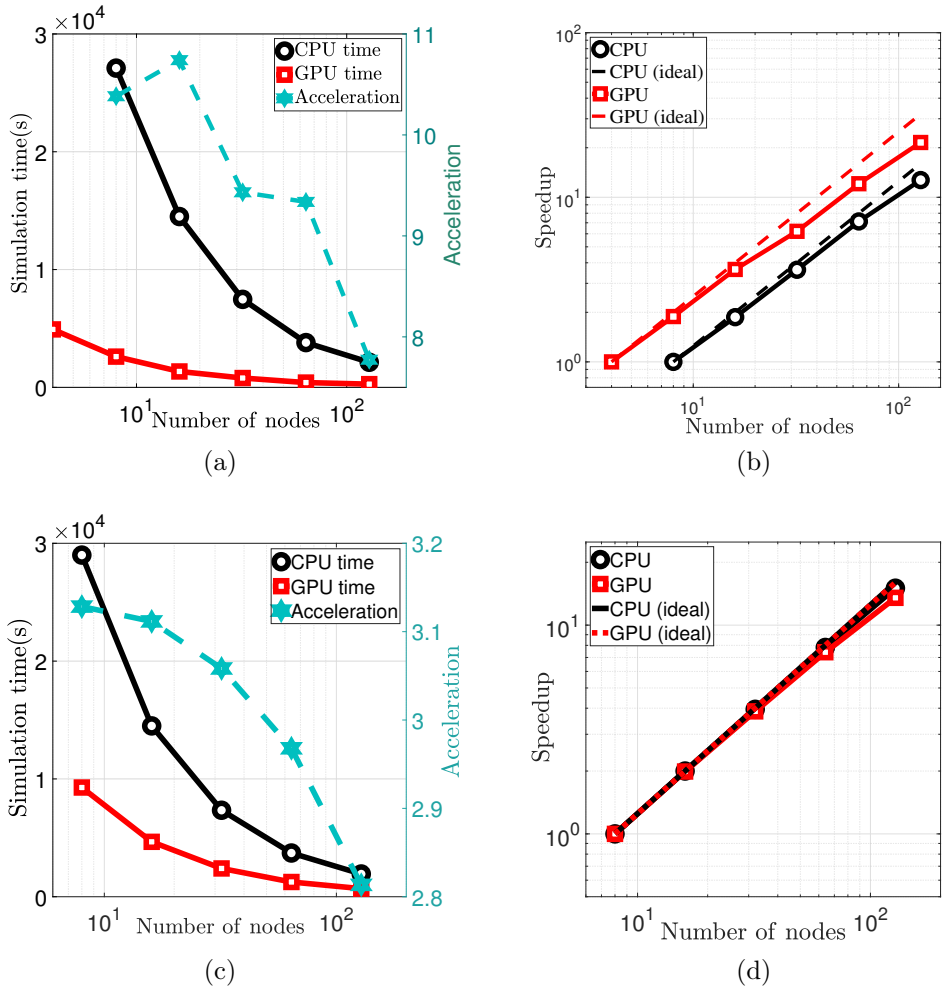

Figure 4: Simulation time (left frames) and speedup (right frames) for circular geometry (top frames) and reconstructed magnetic equilibrium of DIII-D tokamak (bottom frames) as a function of the number of nodes for CPU (black curves) and GPU (red curves) partitions on Jean-Zay supercomputer.

resulting from considering realistic D-shape equilibria (here the magnetic equilibrium for DIII-D tokamak). This is important since for realistic equilibria, verifications of the position of the particles with respect to the magnetic axis and the last magnetic surface must be done at each time step, which may decrease the performance of the code. We analyse on one hand the acceleration obtained when using GPUs with respect to the case where only CPUs are used. On the other hand, we compute the speedup. Both analyses are done for circular analytic (Figs. 4a and 4b) and non-circular (Figs. 4c and 4d) magnetic equilibria when varying the number of computational nodes, using $N_p \sim 2.7 \times 10^8$ particles. On the left panels of Fig. 4 we represent the simulation time on the left y axis as a function of the number of nodes for both pure MPI on CPU (black curves) and hybrid MPI-OpenACC on CPU-GPU (red curves) parallelizations.

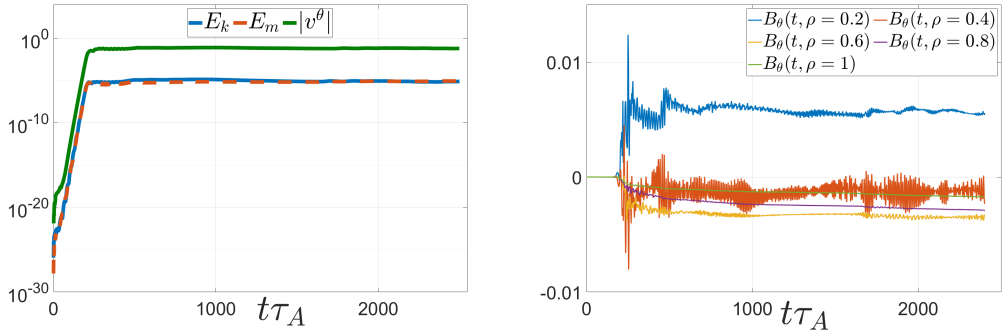

(a) (b)

Figure 5: Left frame: the temporal evolution of magnetic energy (orange curve), kinetic energy (blue curve), and zonal flow (green curve). Right frame: the variations in the amplitude of the poloidal magnetic field at different radial positions.

The acceleration factor is shown on the right y axis. On the right panels of Fig. 4, the speedup is represented. An acceleration factor within the range of $[7.75-11]$ is obtained for the analytic equilibrium for which the parallelized 3D B-splines were used to interpolate the fields at the particle positions. The code exhibits also a significant acceleration factor, within the range of $[2.8-3.15]$, when experimental equilibria is used. The reduced acceleration factor with respect to the circular geometry [27] is due to the special treatment of particle trajectories near the magnetic axis and close to the last magnetic surface.

3. FAR3d simulation of high-β NBI-induced Alfvén Eigenmode activities

In this section, we briefly outline the results of FAR3d simulations that have been employed in TAPAS to investigate the dynamics of energetic particles in the presence of Alfvén eigenmodes. FAR3d solves a set of four reduced equations for thermal plasma: Ohm's law, the toroidal vorticity equation, an equation for pressure, and an equation for parallel velocity. For the EP population, FAR3d solves a system of two equations—the density equation and the parallel velocity equation—derived by taking the moment of the gyrokinetic equation and applying the two-pole energetic ion closure model [41] to include wave-particle interactions. Fields are represented in Fourier space using sine and cosine components. For example, for the electrostatic potential Φ, modes with $n>0$ and $m>0$ correspond to $\sin(m\theta+n\zeta)$, while modes with $-n<0$ and $-m<0$ correspond to $\cos(m\theta+n\zeta)$

$$\Phi=\sum_{m,n}\Phi^s_{mn}\sin(m\theta+n\zeta)+\sum_{m,n}\Phi^c_{mn}\cos(m\theta+n\zeta) \tag{19}$$

To study the transport of EPs, a nonlinear simulation has been performed with FAR3d [22] to investigate the behavior of Alfvén eigenmodes in the presence of

energetic particles (Deuterium) resulting from NBI heating. Magnetic equilibrium was computed using VMEC [37], incorporating up to 15 poloidal mode numbers. The equilibrium calculations were performed under fixed boundary conditions, where the Fourier components of both R and Z corresponding to the last closed magnetic surface of the plasma discharge #159243 were prescribed. The other equilibrium profiles necessary for the numerical reconstruction of the equilibrium were derived from the kinetic EFIT code calculations [42], while the initial profiles for energetic particle density and temperature were obtained from TRANSP [43].

In the FAR3d simulation, the energetic particle temperature peaks at the magnetic axis ($T_{\rm EP}$ = 21 keV) with $\beta_{\rm EP}$ = 3%, while the thermal plasma temperature remains around $T_{\rm th} \approx 2.1$ keV (see [28]). During this nonlinear simulation, 139 Fourier mode m/n pairs were chosen: $n = 0$ ($m = -14 \rightarrow 14$), $n = 3$ ($m = -20 \rightarrow 20$), and $n = 6$ ($m = -52 \rightarrow -18$ and $18 \rightarrow 52$). These mode numbers were determined through previous linear stability analysis with FAR3d, which showed that the dominant modes span $n = 1 \rightarrow 6$ for various linear simulations with different values of β_{EP} [28]. It was observed that the $n = 3$ toroidal mode family exhibits the largest growth rate, hence its selection. Meanwhile, the choice for the $n = 6$ mode family stems from the instability of its associated modes for large values of β_{EP}, which applies to the nonlinear simulation we performed.

The electromagnetic fields from FAR3d were saved at each time step, i.e. $\mathrm{d}t = 0.025\tau_A$ in order to have enough resolution for the particle trajectory integration in TAPAS. Fig. 5a shows the temporal evolution of electromagnetic and kinetic energies of the thermal plasma, represented by the dashed orange and solid blue curves, respectively. Additionally, it illustrates the behavior of the zonal flow structure, indicated by the green curve. As expected, the evolution of thermal plasma energies unfolds in three distinct stages: the initial phase, which corresponds to very small amplitude perturbations before the emergence of various unstable modes, extends until $t = 100\tau_A$, an intermediate linear phase until $t = 224\tau_A$, characterized by the exponential growth of unstable modes, implying energy exchange between energetic particles and the background thermal plasma, and a third phase showing the nonlinear saturation of unstable modes and persisting until the end of the simulation at $t = 2500\tau_A$. Throughout both the linear and the nonlinear phases of these unstable modes, the interaction between Alfvén eigenmodes and energetic particles may result in significant losses of energetic particles, and thus degrade the confinement performance which is discussed later.

As shown in Fig.5a, the evolution of zonal flows also follows similar pattern as that observed for the energies. These zonal flows are defined by the poloidally and toroidally averaged poloidal velocity, i.e. $\langle v^\theta \rangle_{\theta,\varphi} \approx \frac{\partial \tilde{\Phi} m=0,n=0}{\partial \rho}$, and can play a key role in the transport of energetic particles [44].

Fig. 5b illustrates the time evolution of the amplitudes of the poloidal component of the magnetic perturbation at several radial positions. The amplitudes increase as the system enters into the saturation phase, but the growth rate differs at different radial locations, with the most significant increase occurring near the magnetic axis at $\rho = 0.2$,

where $\rho = r/a$ is the normalized minor radius. The behaviour in regions beyond $\rho = 0.4$ is quasi-steady, indicating that the amplitude of the poloidal magnetic field does not exhibit sudden changes in time, the so-called MHD bursts.

In contrast, this quasi-steady behaviour is not observed in the inner plasma, as shown by the blue and orange curves in Fig. 5b for $\rho = 0.2$ and $\rho = 0.4$, respectively. At these specific locations, we observe quasi-steady behaviour for extended time intervals, followed by MHD burst events characterized by abrupt fluctuations in the amplitudes. During these events, the amplitudes increase and subsequently return to their values prior to the event. The occurrence of these MHD bursts at these specific locations is correlated with the of Alfvén eigenmode activity in those regions, as depicted in Figs. 6 and 7. The amplitude of the MHD bursts is decreased when reducing β_{EP} and they may be entirely suppressed for $\beta_{\mathrm{EP}} \leq 1\%$ [28].

Fig.5 also highlights two essential considerations regarding the coupling of FAR3d and TAPAS. First, the energy evolution curves show all characteristic times involved in the dynamics. Second, the time evolution of the amplitude of the fluctuation of the poloidal component of the magnetic field (i.e., Fig.5b) gives access to the shortest characteristic time scales in the studied scenario, given that the amplitude values are saved at each time step. TAPAS time step, therefore, should be smaller than the shortest timescale (τ_s) observed in FAR3d. In this paper, this condition is satisfied, as the characteristic frequency in TAPAS is the gyro-frequency time $\omega_{\mathrm{c,ref}} \approx 10^3 \tau_s^{-1}$. Then, at time t_n, the electromagnetic perturbation is linearly interpolated using its values at t_{prev} and t_{next}, satisfying $t_{\mathrm{prev}} \leq t_n \leq t_{\mathrm{next}}$, and which are computed externally by FAR3d.

Fig.6 presents different time snapshots of the perturbations of the electrostatic potential (top frames) and the radial component of the magnetic field (bottom frames) in the poloidal plane ($R - Z$) where R and Z are dimensional here. These fields are computed at three distinct times: $t = 185\tau_A$ (left column), $t = 460\tau_A$ (middle column), and $t = 1930\tau_A$ (right column). These time instances were deliberately selected during the linear growth phase of unstable modes, the early stages of the nonlinear phase, and late stage in the saturation phase at a time coinciding with an MHD burst event occurring around $t = 1930\tau_A$.

During the linear phase of the simulation, the dominant mode pairs were 9/3, $-9/-3$, 10/3, and $-10/-3$, all of which were localized near the magnetic axis within the inner region of the plasma as shown in Fig. 7a. This concentration is also evident in the profiles of Φ and B^{ρ} presented in Fig. 6. However, it is challenging to distinguish between these different modes in these profiles because they are localized in the same region, with their extrema occurring nearly simultaneously (see Fig. 7a). This mode localization explains why MHD burst events occur at radial positions within the inner plasma, as demonstrated in Fig. 5b.

The nonlinear evolution is characterized by the contribution of other modes, as can be observed in Fig. 8, where we plot the kinetic energy of thermal plasma (8a), its magnetic energy (8b), and the energetic particle energy (8c) for the first 10

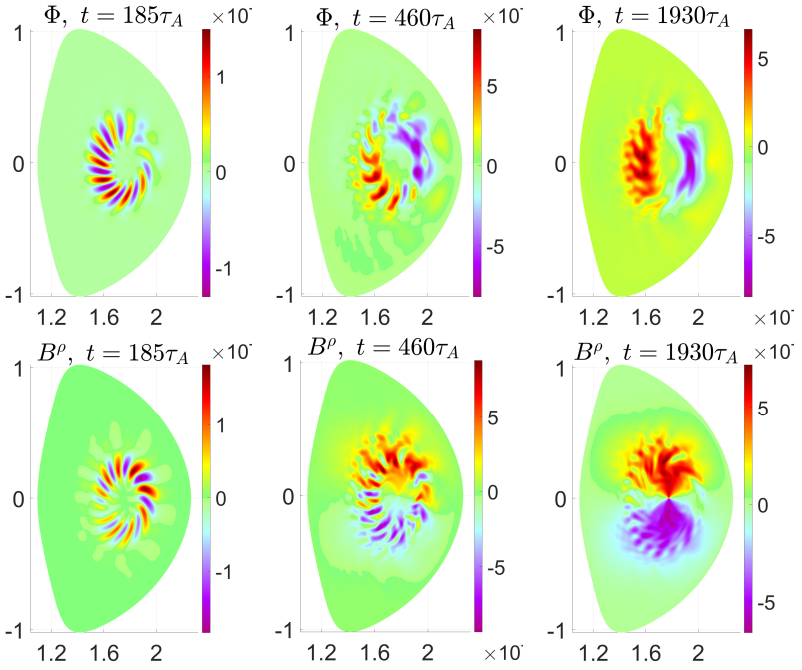

Figure 6: Electrostatic perturbation (top frames), and radial component of the magnetic field (bottom frames) at three different times: the linear phase (left), the initial stage of saturation phase (middle), and a later stage of saturation phase (right), as obtained from FAR3d simulations of Alfvén eigenmodes.

dominant Alfvén eigenmodes (i.e. excluding modes with $n = 0$). As shown in the figure, although the mode 9/3 appears as the dominant one, the contributions of other modes become evident and cannot be neglected. Theses contributions are further evidenced by illustrating their spatial profiles in Fig. 7 at different time instances during the linear phase and the saturation phase, where we observe contributions from other modes, including 11/3, $-11/-3, 1/0, -1/0$, in the non-linear phase of the simulation.

In summary, FAR3d simulations performed in this study to investigate the nonlinear behavior of Alfvén eigenmodes, utilizing the DIII-D equilibrium of discharge #159243 with $\beta_{\mathrm{EPs}} = 3\%$, indicate that both the linear and nonlinear phases are mainly dominated by modes $(m, n) = 8/3,\ 9/3,\ 10/3$ and $11/3$. Furthermore, the temporal evolution of fluctuations in the poloidal magnetic field reveals the emergence of MHD bursts characterized by sudden increase in amplitude. This increase is found to be associated, as will be discussed in a forthcoming paper, with an increase in the radial flux of energetic particles toward the last closed magnetic surface, implying thereby larger particle losses compared to scenarios where MHD bursts do not exist (when β_{EP} is below a critical value).

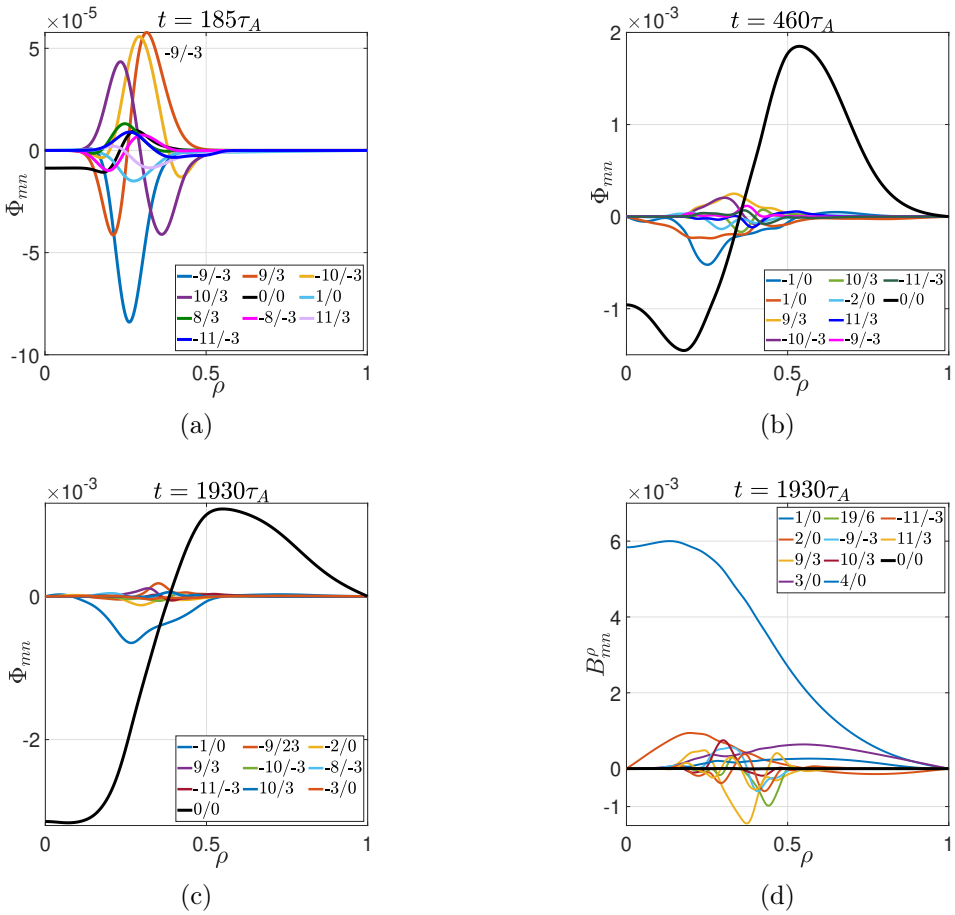

Figure 7: The first ten dominant Fourier mode pairs (m/n) of the electrostatic potential as obtained from FAR3d simulation at three distinct times: the linear phase (a), the initial stage of saturation phase (b), and a later stage of saturation phase (c).The magnetic perturbation is also shown at the later stage (d)

4. Transport and losses of energetic Deuterium with TAPAS

The 3D electromagnetic perturbations obtained with FAR3d have been introduced in TAPAS to investigate the impact of Alfvén eigenmode activities on the dynamics of energetic particles initialized at different energies and radial positions. The study conducted with TAPAS involved mono-energetic particle beams uniformly initialized in poloidal and toroidal directions, as well as in the cosine of the pitch angle (i.e., $-1 \leq \lambda \leq 1$). While the radial initialization was also uniform, the particles were initialized in two different radial intervals for different simulations: $0.038a \leq \rho \leq 0.3a$ (hereafter, the inner region) and $0.3a \leq \rho \leq 0.57a$ (hereafter, the outer region). In TAPAS units, these radial intervals are equivalent to $10 \leq r/\rho_{\rm ref} \leq 80$ and $80 \leq r/\rho_{\rm ref} \leq 150$, respectively. This radial initialization was selected to involve regions where AEs activity is more pronounced, while also expanding two radial intervals: one near the magnetic

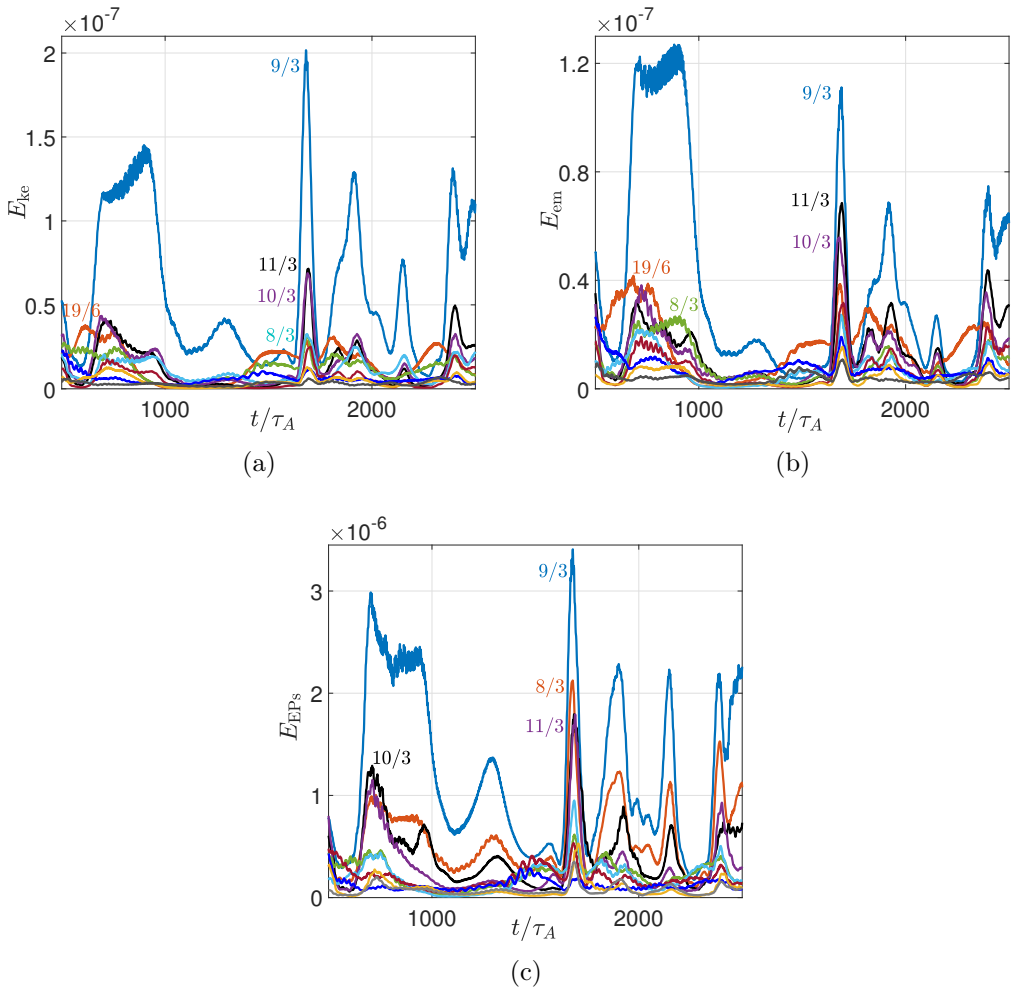

Figure 8: Kinetic (top left) and magnetic (top right) energies for the first 10 dominant Alfvén eigenmodes in the thermal plasma, and energies of EPs for the first 10 dominant modes (bottom).

axis and another situated farther from it. The simulations covered two energy levels ($E_{\mathrm{EPs}} = 65E_{\mathrm{th}}$ and $E_{\mathrm{EPs}} = 115E_{\mathrm{th}}$), where $E_{\mathrm{th}} \approx 2$ keV is the thermal energy of the background plasma. Each simulation was performed first with only the magnetic equilibrium and then taking into account the perturbation from FAR3d. This was done in order to assess the impact of the perturbation on the particle dynamics. Also each simulation was performed with and without collisions. In simulations that include collisions, the characteristic time of the stochastic part of the collision operator was $\tau_c = 10^3 \tau_{\mathrm{TAPAS}} \approx 10^{-6}$s, leading to a time step in Eq. (9) that is 1000 times larger than that used to integrate particle trajectories. Eight simulations for each energy were performed, with $N_p = 1.6 \times 10^6$, resulting in a total of 16 simulations.

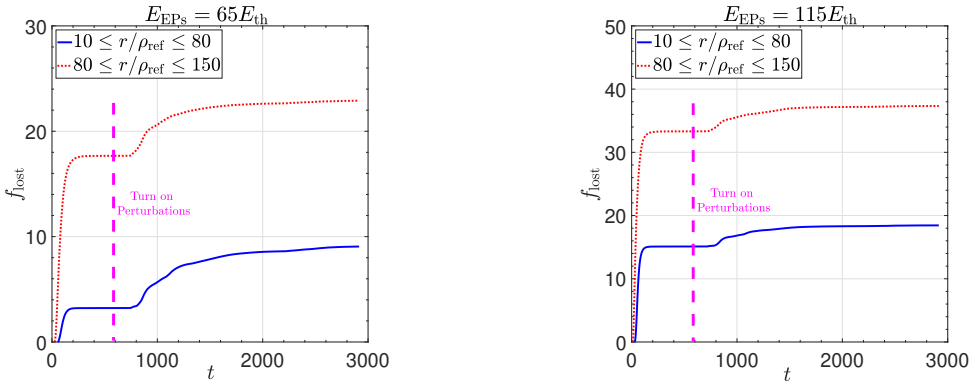

Figure 9: Fraction of lost particles, defined as $f_{\mathrm{lost}} = \frac{N_{\mathrm{p,lost}}(t_{\mathrm{end}})}{N_p} \times 100\%$, for different energies and radii. The vertical line indicates the moment electromagnetic perturbations were initiated, prior to which only prompt losses were present.

4.1. Prompt Losses

Fig. 9 shows the time trace of the fraction of lost particles in the absence of perturbations (up to the vertical dashed line) and when the perturbations are introduced (after the vertical dashed line). It is observed that for both simulated energies almost all the losses occur before $t = 300\tau_A$ and that particles initialized in the outer region exhibit larger losses, as expected. The top frames of Fig. 10 show the fraction of lost particles at the end of various simulations as a function of the initial parallel velocity of the particles. As shown by the blue curves, for both simulated energies, the average value of $v_{\|}$ for lost particles peaks at a value of $5v_{\mathrm{th}}$. However, while lost particles at higher energy ($E_{\mathrm{EPs}} = 115E_{\mathrm{th}}$) explore a wider interval in $v_{\|}$ for the initialization in the inner region, this interval remains narrow compared to the case when particles are initialized in the outer region, as illustrated by the red curves in the top frames of Fig.10. This indicates that the main part of losses might result from trapped particles and that with an increase in the energy passing particles exhibit more significant losses. This is clearly observed in Fig.11, where the fraction of lost particles is given depending on the class of trajectory. The blue bars correspond to the fraction of different particle types, whereas orange bars represent the corresponding prompt losses of these particles. It is observed that prompt losses exhibit dependence on particle type, energy, and radial initialization. Lower-energy prompt losses are dominated by trapped particles for both radial initializations. Conversely, for higher energies, the contribution of co-passing and counter-passing particles to the losses becomes more pronounced when particles are initialized farther from the magnetic axis. The effects of collisions in the investigated regime were found to be negligible due to their longer characteristic time and the duration of the time window of the nonlinear simulations.

A straightforward implication of assuming a strong guide field is the conservation of the magnetic moment (i.e., $\mu = E_{k,\perp}/B$). Consequently, plotting the $2D$ distribution of the number of lost particles as a function of their initial $v_{\|}$ and μ is more insightful.

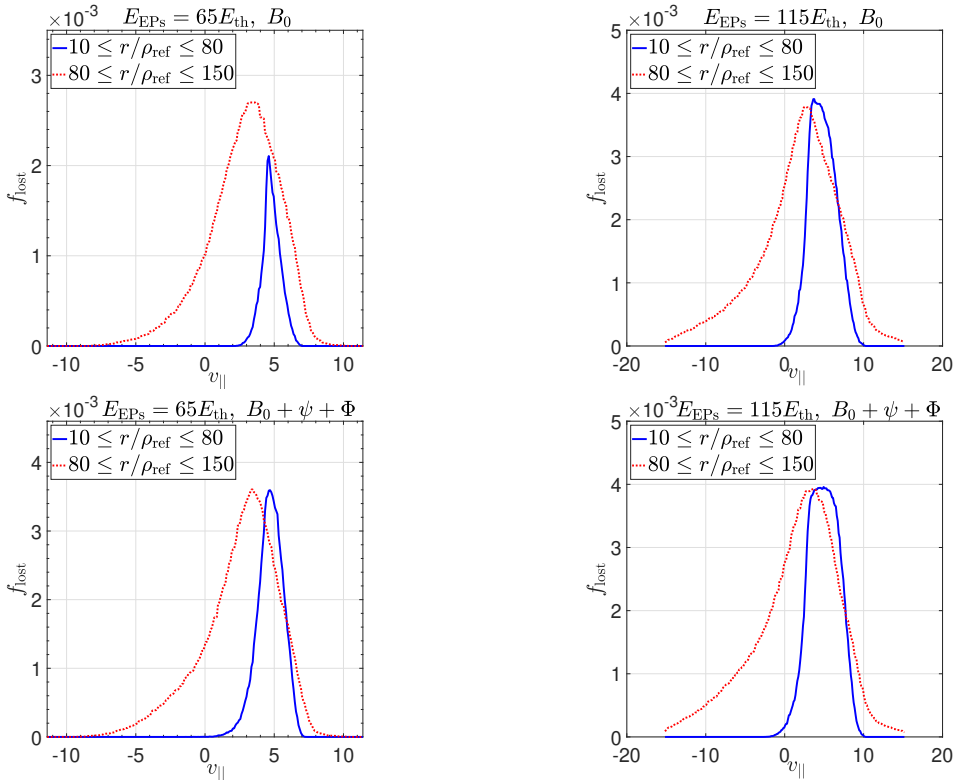

Figure 10: Fraction of lost particles $f_{\text{lost}} = \frac{N_{\text{p,lost(t}_{\text{end}})}}{N_p}$. The left frames correspond to lower energy, and the right ones to the higher energy. In the top frames, only the magnetic equilibrium is considered, while in the bottom frames, electromagnetic perturbations were included.

In the top frames of Fig.12, we plot the number of lost particles in the initial $v_{\|} - \mu$ plane of the phase space for $E_{\text{EPs}} = 115E_{\text{th}}$, for the two radial initializations. The top-left frame corresponds to the inner region initialization, while the top-right frame represents the outer region initialization. In both cases, the majority of losses are from trapped particles, particularly those with large perpendicular energy, as evidenced in the top right frame. On the bottom frames of Fig. 12 we plot the number of lost particles as a function of r/ρ_{ref} and $v_{\|}$. It is observed that particles initialized further from the magnetic axis explore broader ranges along the $v_{\|}$ direction in phase space and exhibit larger losses.

4.2. Transport and losses of energetic particles in the presence of Alfvén eigenmodes

In this section, we investigate the losses that occur after the prompt losses are saturated. To achieve this, the same series of simulations as in the previous subsection were performed including the electromagnetic perturbations from FAR3d. The effect of perturbations is illustrated in Fig. 9 for $E_{\text{EPs}} = 65E_{\text{th}}$ (left) and $E_{\text{EPs}} = 115E_{\text{th}}$ (right). For $E_{\text{EPs}} = 65E_{\text{th}}$, the total losses at the end of the simulations are approximately 9% (blue curve) for the radial initialization in the inner region and 23% (red-dashed curve)

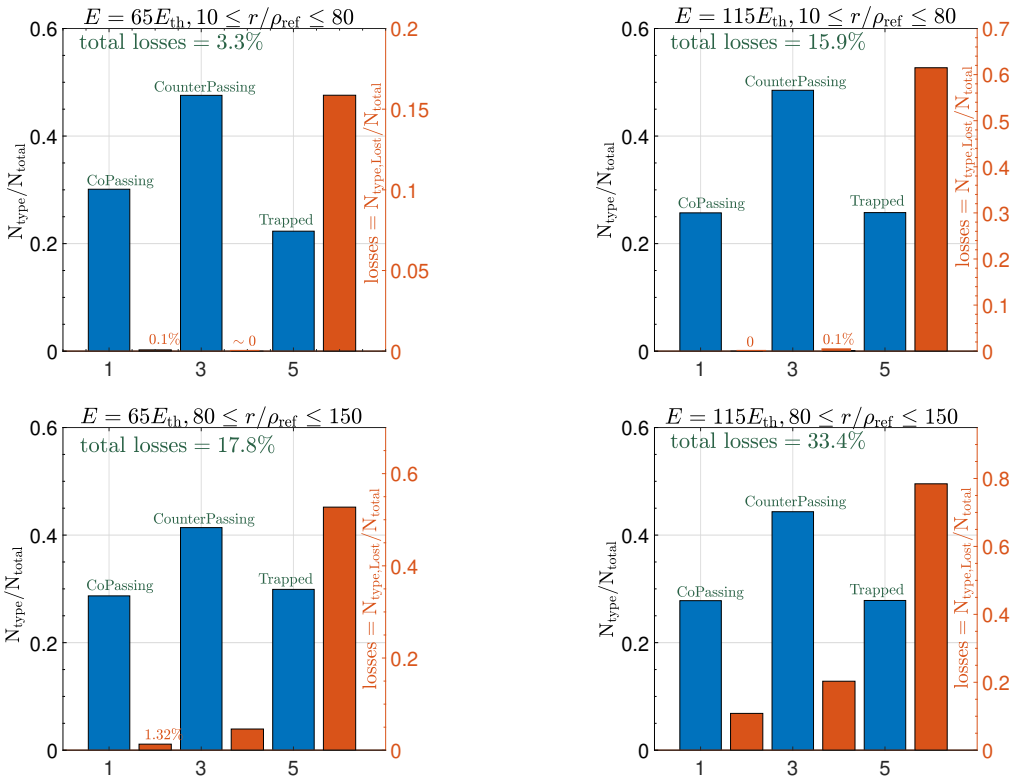

Figure 11: The blue bars represent the fraction of the different classes of trajectories that are present in the initialized particles, depending on the energy and on the radial interval where particles are initialized. For example, there is 30% of co-passing, 47% of counter-passing and 23% of trapped particles in the population with $E = 65E_{th}$ initialized in the inner region. The fraction of prompt losses for each type of trajectory is represented by the orange bars. These losses are calculated as the number of lost particles of a specific class divided by the total number of particles of that class.

for that in the outer region. In comparison to prompt losses, this implies that in this case, the increase in losses due to the presence of AEs activities is 5.8% and 5.2% for the radial initializations in the inner region and the outer region, respectively. On the other hand, the losses at the end of simulations for $E_{EPs} = 115E_{th}$ (right frame of the figure) are 18.4% (blue curve) for the inner region with an increase of around 2.5% compared to prompt losses, and 37.3% (red-dashed curve) for outer region initialization with an increase of around 3.9% compared to the prompt losses. Moreover, the presence of perturbations results in increased losses expanding over a wider range in initial parallel velocity for relatively low energy ($E = 65E_{th}$), as can be observed in Fig. 10. For higher energy, such effect is less evident though and is mainly observable for the initialization in the inner-region.

To further quantify the differences in losses due to the presence of AEs, we plot in Fig. 13 on a log scale the number of lost particles resulting only from the inclusion of the perturbations ($N_{p,lost\ EMs}$) at the end of simulations for $E_{EPs} = 115E_{th}$. In the top

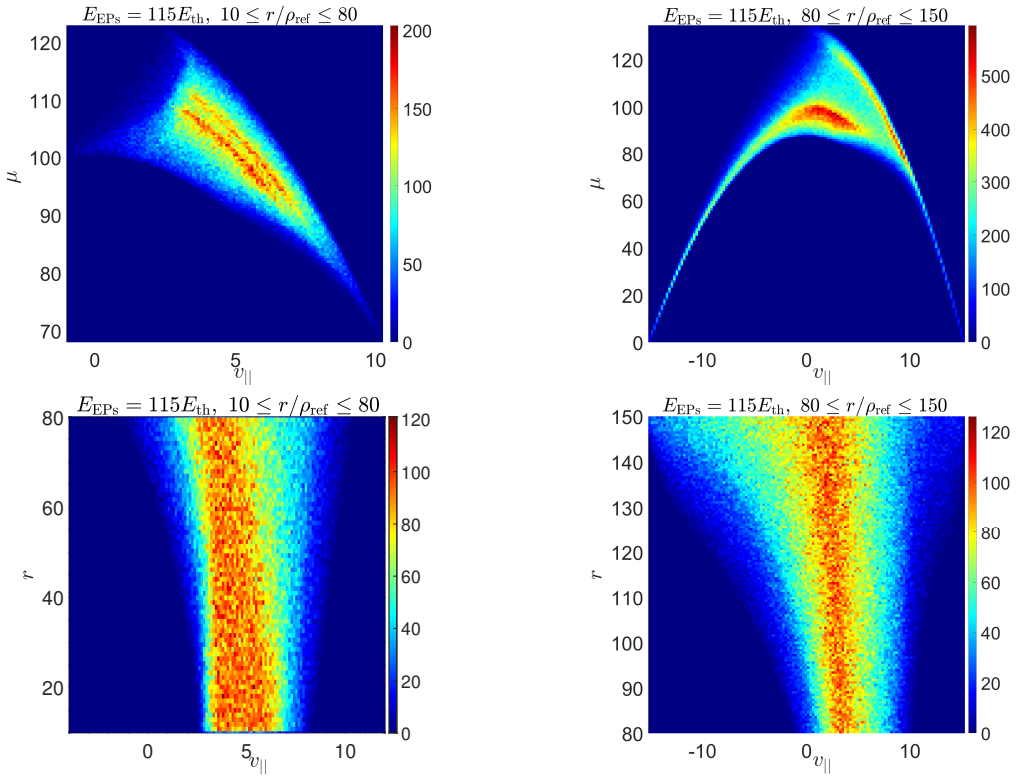

Figure 12: Top frames: number of lost particles as a function of $v_{||}$ and μ for initialization in the inner (left) and outer (right) regions. Bottom frames: number of lost particles as a function of $v_{||}$ and r for initialization in the inner (left) and outer (right) regions.

frames, we show $N_{\text{p,lost EMs}}$ as a function of the initial parallel velocity and magnetic moment for both radial initializations in the inner and the outer regions in the left and right frames, respectively, while in the bottom frames, we plot $N_{\text{p,lost EMs}}$ as a function of the initial parallel velocity and radial position.

Fig. 13 reveals that for the initialization closer to the magnetic axis (left frames), the main contribution to the losses in the presence of AEs is due to the trapped particles and co-passing particles, as evident in the top-left frame where we observe an enhancement in the losses of trapped particles ($v_{||} \le 5$) and co-passing particles ($v_{||} \ge 5$). This result is consistent with the losses of different types of particles shown in the top-right frame of Fig. 11, where significant prompt losses (60%) of the trapped particles were observed (see also Fig. 10). This leads to the conclusion that the enhancement of the losses, shown as two clusters in the top-left frame of Fig. 13, is primarily due to contributions from the trapped particles (the middle cluster) and co-passing particles (the cluster on the right for $v_{||} \ge 5$). On the other hand, co- and counter- passing particles have a larger contribution to the losses when initialized in the outer region, as illustrated in the top right frame of Fig. 13. This result can be understood for the scenarios discussed in this paper since lost particles explore a wider range of $v_{||}$ when initialized further from the magnetic axis, as shown in the bottom frames of Fig. 13. The additional losses can

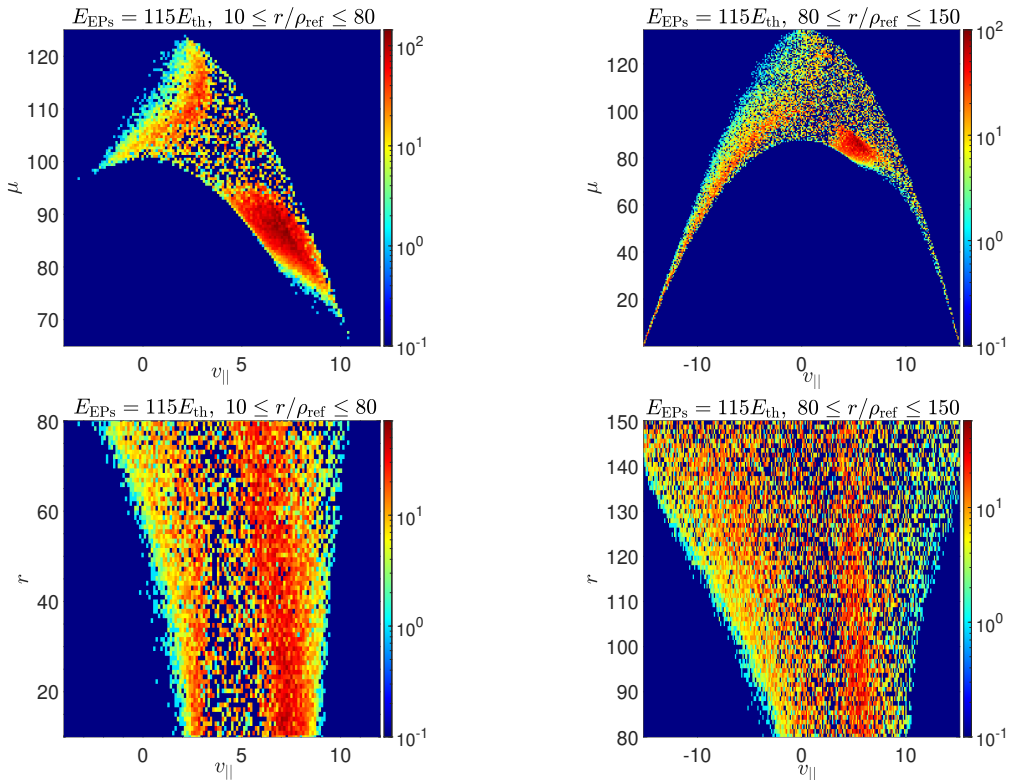

Figure 13: Effect of electromagnetic perturbations on particle losses for $E_{\rm EPs} = 115E_{\rm th}$ as a function of $v_{||}$ and μ (top farmes), and of $v_{||}$ and r (bottom frames).

then be partially attributed to passing particles whose first orbits intersect with the last available closed magnetic surface, a result that also applies when only the prompt losses are considered, as shown in Fig. 11.

The influence of AEs on the spatial distribution of particles is illustrated in Fig.14. In the top frames, we show the number of confined particles at the end of the simulations as a function of the minor radius r for $E_{\rm EPs} = 115E_{\rm th}$ and the two radial initializations considered in this paper. Solid lines represent the case where only the magnetic equilibrium is considered, while the dashed curves correspond to the simulations where electromagnetic perturbations were included. In the investigated scenarios of this paper, we notice that the effect of magnetic equilibrium is to redistribute the particles in the radial direction. It is evident then that the presence of AEs results in more losses, as shown by the dashed curves in the top frames. However, although these losses are small compared to the prompt losses (solid curves) as discussed above (see right frame of Fig. 9), we notice that the interval around the region with the maximum number of particles exhibits the largest losses since the fraction of particles with the largest energies exists in this region. Additionally, we recall that the duration of the AEs simulations performed here is fixed by the external simulation (i.e., in our case, FAR3d code as discussed in section 3). The results reported in Fig. 9 correspond to FAR3d simulations extending over $2500\tau_A = 0.7$ msec, where in these simulations $\tau_A = 2.97\times10^{-7}$sec, which can be very

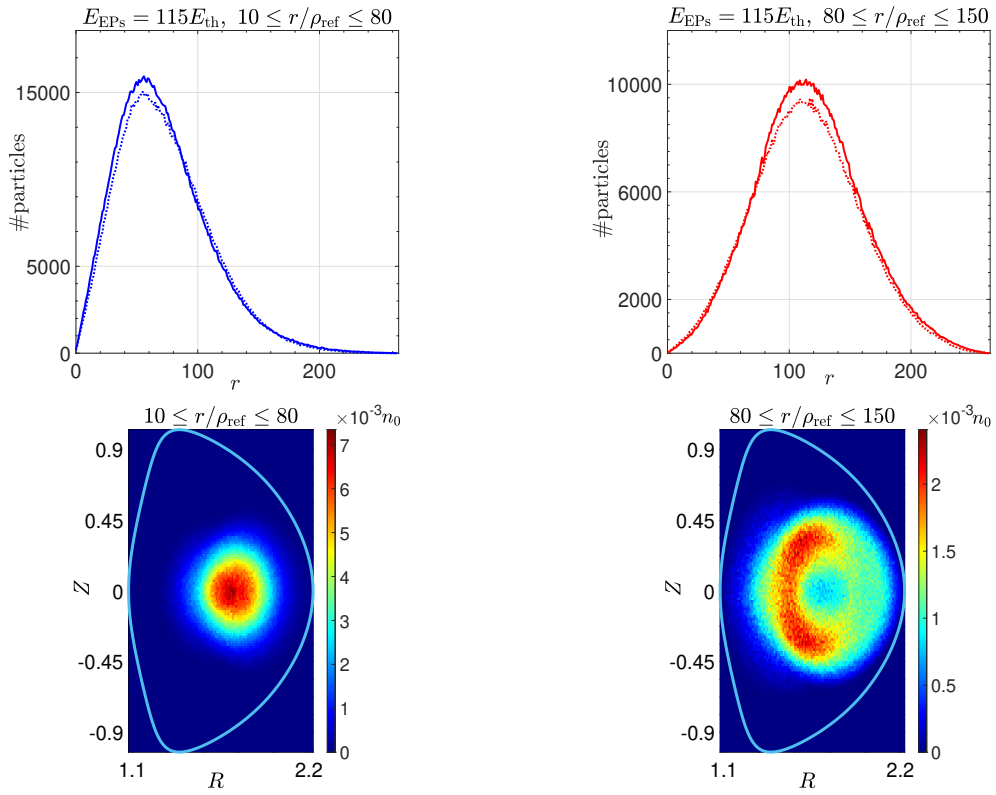

Figure 14: Top frames: the number of confined particles as a function of r for $E_{\mathrm{EPs}} = 115E_{\mathrm{th}}$ (solid and dashed curves represent cases where only the magnetic equilibrium and when AEs are included, respectively). Bottom frames: the number density of confined particles at the end of the simulations in the presence of AEs activities.

short compared to the duration of an AEs pulse that can last for a fraction of second [19]. Therefore, with longer simulations, it is expected that the losses of energetic particles will possibly further increase due to the wave-particle interactions between energetic particles and the AEs.

Another way to visualize the spatial distribution of confined particles is by plotting the normalized energetic particle number density (i.e., $n_{EPs}(R, Z)$) in the poloidal plane at the end of simulations in which electromagnetic perturbations were included, as shown in the bottom frames of Fig.14. In the bottom left frame of the figure, n_{EPs} is displayed for the radial initialization in the inner region, while the bottom right frame presents n_{EPs} for the initialization in the outer region. These frames illustrate that the particles are redistributed in the poloidal plane, with the maximum value of the density, occurring approximately at the average value of the initial radial interval with larger values of density on the high-field side of the poloidal cross-section, a trend that becomes more pronounced when particles are initialized further from the magnetic axis.

5. Conclusions and future work

Recent upgrades implemented in the TAPAS code were presented. These updates include a full-orbit version of the code to resolve particle dynamics in the $6D$ phase space implemented using the Boris scheme to solve the equations of motion for charged particles. Additionally, the code was extended to handle realistic geometries with coordinate systems based on magnetic equilibrium obtained through approximate analytical solution (e.g., analytical solutions of the Grad-Shavranov equation using expansion methods [45]), numerical methods (e.g., employing the VMEC code [37]), or experimental data (e.g., fitting experimental data with TRANSP [43] and EFIT [46]). The new updates also included the implementation of the Metropolis-Hastings sampling method for initializing particles.Collisions were introduced through an operator acting on particle velocity in phase space. These updates, associated with the newly implemented multi-dimensional bspline interpolation and a correction algorithm near the last available magnetic surface, enabled us to couple TAPAS with other codes, such as the gyro-fluid code FAR3d [47] or the full-f GYSELA code [40].

Coupling TAPAS with FAR3d, we studied the transport and losses of EPs in the presence of Alfvén eigenmodes in the DIII-D tokamak. FAR3d simulation was performed for $\beta_{EP} = 0.03$. Linear analysis revealed that within this phase, the $n = 3$ EAE family at $f \approx 160\ keV$ exhibited the maximum growth rate and was prominently dominated by 9/3, 10/3, and 11/3 modes; while the nonlinear phase, characterized by MHD burst events, possibly resulting from modes overlap, was primarily dominated by the 9/3 RSAE mode [28].

In TAPAS, the particles were mono-energetic and uniformly initialized in both toroidal and poloidal angles for two radial initializations: $10 \leq r/\rho_{\text{ref}} \leq 80$ and $80 \leq r/\rho_{\text{ref}} \leq 150$. We have shown that the prompt losses (i.e. first orbit losses) of energetic particles are larger for higher energies and when initialized further from the magnetic axis. As expected, the prompt losses strongly depend on the particle type, while the effect of collisions on the losses was negligible for the time window simulated.

In the presence of AEs activities, the effect of collisions remains negligible. Also, the losses of energetic particles increase with the inclusion of electromagnetic perturbations for low and high energies. This rise in losses is primarily attributed to the enhancement in trapped particle losses (as classified with respect to equilibrium) and contributions resulting from passing particles,. Moreover, the ratio between losses resulting from AEs activities and the prompt losses was larger for energetic particles with lower energy since the prompt losses of trapped particles in this case were smaller compared to energetic particles with higher energy.

The simulations performed in this paper, aimed at testing the new tools developed in TAPAS to account for realistic geometries and to investigate energetic particle transport in 6D phase space by adopting simple uniform initialization of mono-energetic particles in phase space. Further simulations with more realistic particle initialization are necessary to model experiments. This includes simulating parallel and perpendicular

Neutral Beam Injection (NBI) at specific toroidal angles, which will require employing the Metropolis algorithm to sample radial profiles of density and temperature for different species. Another crucial aspect is to consider longer nonlinear simulations to study the effect of collisions with the background plasma on the transport of energetic particles, as collisions play an important role in slowing down these particles and consequently affect their losses and transport, depending on their energy and the length of Alfvén eigenmode events.

Acknowledgments

The authors want to thank W.W. Heidbrink, M. A. Van Zeeland, D. Spong, and D. Del Sarto for useful discussions. This work has received financial support from the AIM4EP project (ANR-21-CE30-0018), funded by the French National Research Agency (ANR), from the Comunidad de Madrid under the project 2019-T1/AMB-13648, and from the Oak Ridge National Laboratory, managed by UT-Battelle, LLC, for the US Department of Energy under Contract No. DE-AC05-00OR22725. TAPaS simulations were performed on HPC resources of IDRIS under the allocations 2021-A0100512455, 2022-AD010512455R1 and 2023-A0140514165 made by GENCI. TAPaS development, optimization and deployment on GPU accelerator were done within the framework of an advanced support program funded by IDRIS and GENCI.

References

[1] K. McGuire, R. Goldston, M. Bell, M. Bitter, K. Bol, K. Brau, D. Buchenauer, T. Crowley, S. Davis, F. Dylla, H. Eubank, H. Fishman, R. Fonck, B. Grek, R. Grimm, R. Hawryluk, H. Hsuan, R. Hulse, R. Izzo, R. Kaita, S. Kaye, H. Kugel, D. Johnson, J. Manickam, D. Manos, D. Mansfield, E. Mazzucato, R. McCann, D. McCune, D. Monticello, R. Motley, D. Mueller, K. Oasa, M. Okabayashi, K. Owens, W. Park, M. Reusch, N. Sauthoff, G. Schmidt, S. Sesnic, J. Strachan, C. Surko, R. Slusher, H. Takahashi, F. Tenney, P. Thomas, H. Towner, J. Valley, and R. White. Study of high-beta magnetohydrodynamic modes and fast-ion losses in pdx. Phys. Rev. Lett., 50:891–895, Mar 1983.

[2] W.W. Heidbrink and G. Sager. The fishbone instability in the diii-d tokamak. Nuclear Fusion, 30(6):1015, jun 1990.

[3] H.H. Duong, W.W. Heidbrink, E.J. Strait, T.W. Petrie, R. Lee, R.A. Moyer, and J.G. Watkins. Loss of energetic beam ions during tae instabilities. Nuclear Fusion, 33(5):749, may 1993.

[4] H.H. Duong and W.W. Heidbrink. Confinement of fusion produced mev ions in the diii-d tokamak. Nuclear Fusion, 33(2):211, feb 1993.

[5] K Appert, R Gruber, F Troyuon, and J Vaclavik. Excitation of global eigenmodes of the alfven wave in tokamaks. Plasma Physics, 24(9):1147, sep 1982.

[6] T. E. Evans, P. M. Valanju, J. F. Benesch, Roger D. Bengtson, Y. M. Li, S. M. Mahajan, M. E. Oakes, D. W. Ross, X. Z. Wang, J. G. Watkins, and C. M. Surko. Direct observation of the structure of global alfvén eigenmodes in a tokamak plasma. Phys. Rev. Lett., 53:1743–1746, Oct 1984.

[7] G. Y. Fu and J. W. Van Dam. Title of the article. Phys. Fluids B, 1:1919, 1989.

[8] N.N. Gorelenkov, E. Fredrickson, E. Belova, C.Z. Cheng, D. Gates, S. Kaye, and R. White. Theory and observations of high frequency alfvén eigenmodes in low aspect ratio plasmas. Nuclear Fusion, 43(4):228, mar 2003.

[9] C. Z. Cheng and M. S. Chance. Low-n shear Alfvén spectra in axisymmetric toroidal plasmas. The Physics of Fluids, 29(11):3695–3701, 11 1986.

[10] H. Kimura, Y. Kusama, M. Saigusa, G.J. Kramer, K. Tobita, M. Nemoto, T. Kondoh, T. Nishitani, O. Da Costa, T. Ozeki, T. Oikawa, S. Moriyama, A. Morioka, G.Y. Fu, C.Z. Cheng, and V.I. Afanas'ev. Alfvén eigenmode and energetic particle research in jt-60u. Nuclear Fusion, 38(9):1303, sep 1998.

[11] R. Betti and J. P. Freidberg. Ellipticity induced Alfvén eigenmodes. Physics of Fluids B: Plasma Physics, 3(8):1865–1870, 08 1991.

[12] R. Betti and J. P. Freidberg. Stability of Alfvén gap modes in burning plasmas. Physics of Fluids B: Plasma Physics, 4(6):1465–1474, 06 1992.

[13] G. J. Kramer, M. Saigusa, T. Ozeki, Y. Kusama, H. Kimura, T. Oikawa, K. Tobita, G. Y. Fu, and C. Z. Cheng. Noncircular triangularity and ellipticity-induced alfvén eigenmodes observed in jt-60u. Phys. Rev. Lett., 80:2594–2597, Mar 1998.

[14] A. D. Turnbull, E. J. Strait, W. W. Heidbrink, M. S. Chu, H. H. Duong, J. M. Greene, L. L. Lao, T. S. Taylor, and S. J. Thompson. Global Alfvén modes: Theory and experiment*. Physics of Fluids B: Plasma Physics, 5(7):2546–2553, 07 1993.

[15] W. Deng, Z. Lin, I. Holod, Z. Wang, Y. Xiao, and H. Zhang. Linear properties of reversed shear alfvén eigenmodes in the diii-d tokamak. Nuclear Fusion, 52(4):043006, mar 2012.

[16] D.A. Spong. Simulation of alfvén frequency cascade modes in reversed shear-discharges using a landau-closure model. Nuclear Fusion, 53(5):053008, apr 2013.

[17] M. S. Chu, J. M. Greene, L. L. Lao, A. D. Turnbull, and M. S. Chance. A numerical study of the high-n shear Alfvén spectrum gap and the high-n gap mode. Physics of Fluids B: Plasma Physics, 4(11):3713–3721, 11 1992.

[18] WW Heidbrink. Basic physics of alfvén instabilities driven by energetic particles in toroidally confined plasmas. Physics of Plasmas, 15(5), 2008.

[19] S. Sharapov. Energetic Particles in Tokamak Plasmas. CRC Press, 1st edition, 2021.

[20] WW Heidbrink and RB White. Mechanisms of energetic-particle transport in magnetically confined plasmas. Physics of Plasmas, 27(3), 2020.

[21] Y. Todo. Properties of energetic-particle continuum modes destabilized by energetic ions with beam-like velocity distributions. Physics of Plasmas, 13(8):082503, 08 2006.

[22] D.A. Spong, M.A. Van Zeeland, W.W. Heidbrink, X. Du, J. Varela, L. Garcia, and Y. Ghai. Nonlinear dynamics and transport driven by energetic particle instabilities using a gyro-landau closure model*. Nuclear Fusion, 61(11):116061, oct 2021.

[23] Eero Hirvijoki, Otto Asunta, Tuomas Koskela, Taina Kurki-Suonio, Juho Miettunen, Seppo Sipilä, Antti Snicker, and Simppa Äkäslompolo. Ascot: Solving the kinetic equation of minority particle species in tokamak plasmas. Computer Physics Communications, 185(4):1310–1321, 2014.

[24] SH Ward, Rob Akers, AS Jacobsen, P Ollus, SD Pinches, E Tholerus, RGL Vann, and MA Van Zeeland. Verification and validation of the high-performance lorentz-orbit code for use in stellarators and tokamaks (locust). Nuclear Fusion, 61(8):086029, 2021.

[25] R. B. White and M. S. Chance. Hamiltonian guiding center drift orbit calculation for plasmas of arbitrary cross section. The Physics of Fluids, 27(10):2455–2467, 10 1984.

[26] L Carbajal, D del Castillo-Negrete, D Spong, S Seal, and L Baylor. Space dependent, full orbit effects on runaway electron dynamics in tokamak plasmas. Physics of Plasmas, 24(4):042512, 2017.

[27] David Zarzoso, Diego del Castillo-Negrete, Rémi Lacroix, Pierre-Eric Bernard, and Stanislas Touzet. Transport and losses of fusion-born alpha particles in the presence of tearing modes using the new toroidal accelerated particle simulator (tapas). Plasma Physics and Controlled Fusion, 64(4):044003, 2022.

[28] J Varela, D A Spong, L Garcia, Y Ghai, D Zarzoso, D del Castillo-Negrete, H Betar, J Ortiz, D C Pace, M A Van Zeeland, X Du, R Sanchez, V Tribaldos, and J M Reynolds-Barredo. Effect of the neutral beam injector operational regime on the alfven eigenmode saturation phase in diii-d

plasma. Plasma Physics and Controlled Fusion, 65(12):125004, oct 2023.
[29] HIRSHMAN S. P. and Whitson J. C. The Physics of fluids, 26(12):3553–3568, 1983.
[30] PERAZA-RODRIGUEZ H. et al. Physics of Plasmas, 24(8), 2017.
[31] PANICI D. et al. Journal of Plasma Physics, 89(3):955890303, 2023.
[32] HIRSHMAN S. P. et al. Physics of Plasmas, 18(6), 2011.
[33] Julien Derouillat, Arnaud Beck, Frédéric Pérez, Tommaso Vinci, M Chiaramello, Anna Grassi, M Flé, Guillaume Bouchard, I Plotnikov, Nicolas Aunai, et al. Smilei: A collaborative, open-source, multi-purpose particle-in-cell code for plasma simulation. Computer Physics Communications, 222:351–373, 2018.
[34] Nicholas Metropolis and Stanislaw Ulam. The monte carlo method. Journal of the American statistical association, 44(247):335–341, 1949.
[35] Nicholas Metropolis, Arianna W Rosenbluth, Marshall N Rosenbluth, Augusta H Teller, and Edward Teller. Equation of state calculations by fast computing machines. The journal of chemical physics, 21(6):1087–1092, 1953.
[36] W Keith Hastings. Monte carlo sampling methods using markov chains and their applications. 1970.
[37] S. P. Hirshman and J. C. Whitson. Steepest-descent moment method for three-dimensional magnetohydrodynamic equilibria. The Physics of Fluids, 26(12):3553–3568, 12 1983.
[38] Per Helander and Dieter J Sigmar. Collisional transport in magnetized plasmas, volume 4. Cambridge university press, 2005.
[39] Setsuo Ichimaru. Basic principles of plasma physics: a statistical approach. CRC Press, 2018.
[40] V. Grandgirard, J. Abiteboul, J. Bigot, T. Cartier-Michaud, N. Crouseilles, G. Dif-Pradalier, Ch. Ehrlacher, D. Esteve, X. Garbet, Ph. Ghendrih, G. Latu, M. Mehrenberger, C. Norscini, Ch. Passeron, F. Rozar, Y. Sarazin, E. Sonnendrücker, A. Strugarek, and D. Zarzoso. A 5d gyrokinetic full-f global semi-lagrangian code for flux-driven ion turbulence simulations. Computer Physics Communications, 207:35–68, 2016.
[41] C. L. Hedrick, J.-N. Leboeuf, and D. A. Spong. Alpha-Alfvén local dispersion relation and solutions. Physics of Fluids B: Plasma Physics, 4(12):3869–3882, 12 1992.
[42] L.L. Lao, H. St. John, R.D. Stambaugh, A.G. Kellman, and W. Pfeiffer. Reconstruction of current profile parameters and plasma shapes in tokamaks. Nuclear Fusion, 25(11):1611, nov 1985.
[43] Joshua Breslau, Marina Gorelenkova, Francesca Poli, Jai Sachdev, Alexei Pankin, Gopan Perumpilly, Xingqiu Yuan, and Laszlo Glant. Transp, jun 2018.
[44] David Zarzoso and Diego del Castillo-Negrete. Anomalous losses of energetic particles in the presence of an oscillating radial electric field in fusion plasmas. Journal of Plasma Physics, 86(2):795860201, 2020.
[45] J. P. Hans Goedbloed and Stefaan Poedts. Principles of Magnetohydrodynamics: With Applications to Laboratory and Astrophysical Plasmas. Cambridge University Press, 2004.
[46] O. Meneghini, S.P. Smith, L.L. Lao, O. Izacard, Q. Ren, J.M. Park, J. Candy, Z. Wang, C.J. Luna, V.A. Izzo, B.A. Grierson, P.B. Snyder, C. Holland, J. Penna, G. Lu, P. Raum, A. McCubbin, D.M. Orlov, E.A. Belli, N.M. Ferraro, R. Prater, T.H. Osborne, A.D. Turnbull, G.M. Staebler, and The AToM Team. Integrated modeling applications for tokamak experiments with omfit. Nuclear Fusion, 55(8):083008, jul 2015.
[47] J. Varela, D.A. Spong, and L. Garcia. Analysis of alfven eigenmodes destabilization by energetic particles in tj-ii using a landau-closure modela. Nuclear Fusion, 57(12):126019, sep 2017.